DOI: 10.13009/EUCASS2019-206

Microstructural study of nickel-based superalloys through open source software of image analysis.

Ignacio Escobar-Moreno, M. V. Aguirre, Eva-María Andrés-López, Manuel José Viscasillas, Daniel Barba
ignacio.escobar.moreno@alumnos.upm.es
School of Aeronautics and Space Engineering, Technical University of Madrid (UPM)
mariavega.aguirre@upm.es
Technical University of Madrid (UPM); Centro de Investigación de Materiales Estructurales (CIME)

Abstract
The control of materials at the microstructural level is critical for the aerospace sector: the properties of their components are governed by microstructural features usually design with great precision. This is especially the case for Ni-based superalloy, a class of materials used in high-temperature aerospace components. In this work we present an image analysis framework based on open-source software to quantify precisely and efficiently the different microstructural properties of a set of commercial Ni-based superalloys (Inconel-718, HasteloyX, René77 and Inconel-738). The framework is then used to investigate the failure cause of an aerospace component: an auxiliary power unit.

1. Introduction

The macroscopic properties of high-performance materials are usually controlled by what is occurring at the microscale/nanoscale [1,3,7,8,9], see Figure 1. This is because their deformation mechanics are governed by the different phases present at the microscale and their distribution within the material (i.e., microstructure in metals) [4,5,6]. This is specially the case for Ni-based superalloys, a set of high-performance alloys made of Ni and up to a dozen of exotic alloyants used in high temperature performance applications [4]. In these alloys, a careful arrangement of shear resistant γ'-precipitates provides them with unique properties at high temperatures which makes them populate most of the commercial aircraft engines and energy turbine generators [4,2]. The arrangement and fraction of γ' precipitates within the γ matrix is carefully designed to optimise their strength at high temperatures [10,11,12,14]. The advances in the design and control of these precipitates in the last few decades -- supported by new high-resolution characterisation techniques -- have allowed the development of new engines with unprecedent fuel efficiencies [13].

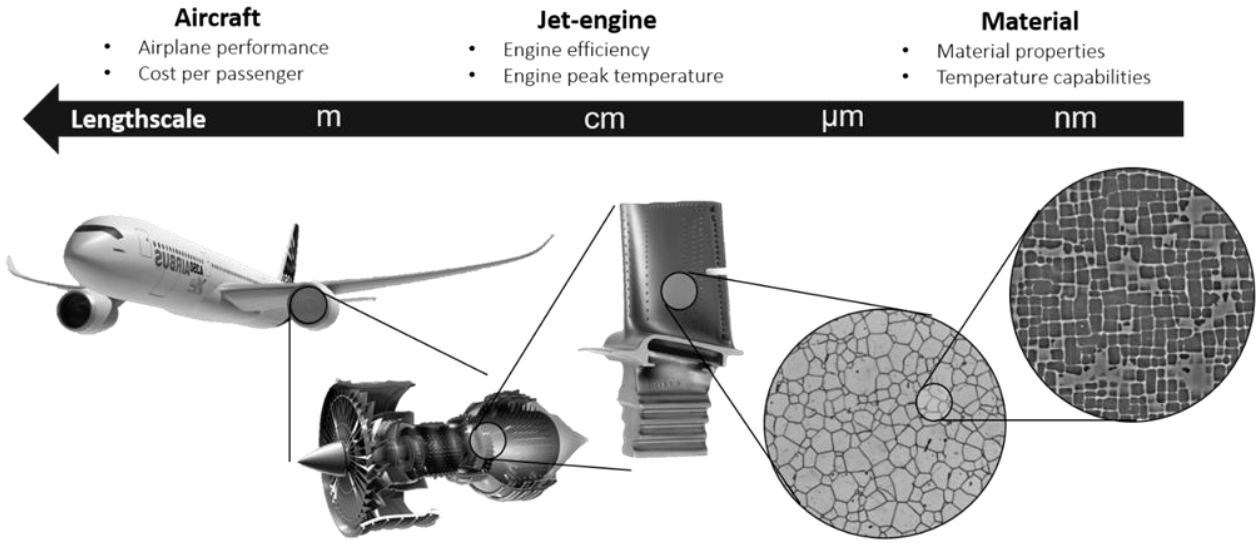

Figure 1: Diagram of the connection between the different scales in materials engineering problems. Quantitative analysis of the microstructure at the lower scale define the performance of the whole component at the larger scale.

DOI: 10.13009/EUCASS2019-206

Therefore, measuring, quantifying and controlling these microstructural features is a critical exercise for metallurgists and materials engineers for any kind of high-performance application [15-22], and more specifically in aerospace components [15-19]. This is defined as quantitative microstructure characterisation.

Processing and image analysis techniques for industrial and scientific environments are relatively recent, their beginnings can be found about 30 years ago, and have evolved rapidly helped by the advance of computers and their computing power. Image analysis can be defined as a software that includes a series of functions and process and measurement tools and make possible that a PC make decisions about image objects. The software is based on a vision system in the interpretation and analysis of pixels, the final result can be, from the measurement of a particle, to the determination of the number of characters in an image [1]. There have been several efforts in the literature regarding the accurate and efficient quantitative analysis of microstructures in metals by image analysis [15-22]. The workflow is usually common: (i) first, microstructural characterisation is done by microscopy methods (i.e., scanning electron microscopy, optical microscopy), (ii) then the images are processed by different filters and (iii) finally, image analysis algorithms are used to quantify the microstructure. Within these works, special mention deserves Payton et al. [19], who use backscattered electron imaging combined selective etching of γ' particles which yields images that can be more readily segmented with image processing algorithms to quantify the microstructural distribution of γ' precipitates. Szczotok et al. [18] present a new method of quantifying the total volume fraction of the γ′-phase applying images filters on a combination of images using light microscopy, scanning electron microscopy (at two-different magnifications) and scanning transmission electron microscopy. Sarosi et al. [16] studied several microstructural quantification techniques using different types of TEM modes images and ranked them. This method depends on the sample thickness, which is really difficult to measure property. To overcome this problem, they propose a new method which relies on average intensities of the chemical elements used to track the precipitates, making the measuring independent on the sample thickness. More recently, Smith et al. [15] present an advanced method combining images at 0° and 180° degree rotation to provide a superior contrast, showing improvements over the previous techniques. They validated the results of their new methods with phase extraction values. All these works represent good examples of the recent advances in the last few years of the techniques and methods used to quantify the microstructure of Ni-based superalloys. These advances has been usually ended embedded in the great amount of professional software which provide image analysis for materials science, medicine or industry, e.g. XPlus-REMET, Axiovision-ZEISS or MIAS 4.0. However, these packages are usually constrained in terms of their versatility and their licenses requires certain level of inversion from research groups. The appearance of open-source software has opened the door to new research possibilities with increased versatility. ImageJ is an example of this open-source software programmed in Java, developed at the National Institutes of Health.

In the current work, the capabilities of this open-source software (ImageJ) have been exploited to present an automated, efficient and precise framework for quantitative microstructural characterisation. We have analysed carefully the effect of different acquisition parameters, i.e. magnification, on the accurate quantification of the microstructure in a polycrystalline Ni-based superalloy. The structure of the paper is as follows: first, we show the power of the tool to extract typical material properties in a set of different Ni-based superalloys (IN718, Hastealloy X and Rene 77). The results obtained using this method are presented, discussed and validated. Then, to demonstrate the power of the framework, we have applied the image analysis framework to a complex engineering problem: the investigation of the failure mechanism of real aerospace component: an auxiliary power unit.

2. Methodology

In the present work, four materials for aero engines are studied. They are used in different aerospace components that withstand severe service conditions:

- Turbine shaft (Inconel 718). As fabricated, non-service condition.
- Combustion chamber (Hastelloy X) with TBC (Zirconia stabilized with Yttria). End of life condition.
- Vane of first stage turbine (René 77). End of life condition
- Centrifugal turbine of an APU (Inconel 738). Service failure

All these are nickel-based alloys, manufactured by wrought (Inconel 718 and Hastelloy X) and casting (René 77 and Inconel 738).
Their nominal compositions are as follows in Table 1:

DOI: 10.13009/EUCASS2019-206

Table 1: Nickel-based alloys composition.

%wt	Cr	Mo	Co	W	C	Mn	Si	B	Nb	Al	Ti	Fe	Others	Ni
Inconel 718 (1)	19	3.1	1		0.08	0.35	0.35	0.006	5.1	0.5	0.9	balance	0.3Cu, 0.05Ta	53
Hasteloy X (2)	22	9	1.5	0.6	0.1	1	1	0.008	0.5	0.5	0.15	18		balance
René 77 (3)	14.6	4.2	15		0.07					4.3	3.3			balance
Inconel 738 (4)	16	1.75	8.5	2.6	0.17			0.01	0.9	3.4	3.4		1.75Ta, 0.1Zr	balance

(1) UPMET; (2) Hynes International; (3) Metal Tek; (4) INCO

2.1. Samples preparation

Longitudinal and transverse samples from the components are obtained by means of disk cutting. These were mounted in epoxy resin to handle. They were prepared by SiC-paper (P100, P200, P400 and P600), polished with diamond slurry (15, 6 and 3 microns) and finished with colloidal silica. Different etchants are used, such as Kalling 2 and Lactic acid. The best results were obtained by etching with lactic acid because this does not dissolve γ' phase.

2.2. Microstructural study

Scanning Electron Microscope (SEM) Hitachi S-3400 with EDX Oxford system were used to analyse composition. Micrographs were obtained using 15 kV and 10mm working distance. For improved image resolution the work distance were reduced at some points. Images obtained with backscattered electron sensors are selected because of their better compositional contrast in order to distinguish γ' precipitates.
Light microscopes (Reichter microscope with Leica digital camera) to obtain micrographs with less magnification to appreciate microstructural characteristics, such as grain size when it is too large for SEM.

2.3. Microstructural analysis

Two open source software are used to analyse microstructure: pre-processing with "GIMP2" (GNU) and analysing with "ImageJ" software (National Institutes of Health). The results accuracy and efficiency of ImageJ depends of the quality of images. GIMP is a user-friendly software that allows an easy work to process the images.

3. Experimental data and results

In this chapter, we show the different capabilities of the Image J software by analysing typical microstructural properties in three different commercial superalloys: Inconel 718, Hastelloy X and Rene 77). These will be the basis of the more complex application of the software (engine failure investigation) presented in the following section. The procedure of the image analysis will be the same for all the studies present in this article. Firstly, using Gimp2 the image is turned into a grayscale image prepared to be analysed by the second program ImageJ, shown in Figure 2.

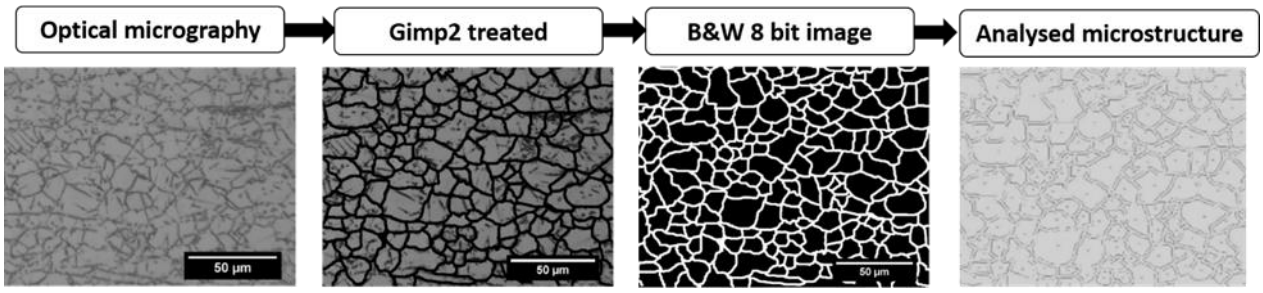

Figure 2: Process flow of the Image analysis framework presented in this work.

DOI: 10.13009/EUCASS2019-206

3.1. Inconel 718

Inconel 718 is a nickel-iron based superalloy used in shafts and blades in aerospace industry. In this case, the open software has been used to estimate the grain and δ phase size. A typical microstructure for this alloy under study is presented in Figure 2. The grain size and geometrical aspects of these grains have been studied. The image particles have been measured by ImageJ, resulting in the outlines in Figure 2. The quantitative results of this analysis are presented in Table 1. The grain size and circularity have been estimated in several different micrographs giving more accuracy to the estimation.

It is important for a correct analysis that the image shows clearly the particles required for the study, as shown in Figure 2-left.

Table 2: Results of Inconel 718 grain size estimation.

Grain Size	Number of elements	Total area [μm^2]	Mean Radius [μm]	Circularity
Micro 1	192	18319.73	5.51	0.61
Micro 2	224	17775.14	5	0.54
Micro 3	296	17609.25	4.35	0.59

The interesting values in Table 2 are the mean radius and circularity. The first parameter give and grain size approximation and latter one shows how similar is the grain to a circle confirming how equiaxial is the grain. The same order of elements is measured; both show similar values in the different micrographics, obtaining a mean radius of 5 μm and a circularity of 0.58.

In addition, the δ phase size, for the same alloy, has been analysed (see results in Table 3). The same procedure of image analysis has been followed. The δ phase appears in the grain edge of the forge alloys and helps to control the grain size, keeping as small-scale as possible.

Table 3: Results of Inconel 718 delta phase size estimation.

Delta phase size	Number of elements	Total area [μm^2]	Mean radius [μm]	Circularity
Micro 1	497	243	0.39	0.39
Micro 2	377	290.3	0.5	0.34
Micro 3	348	152.93	0.37	0.34

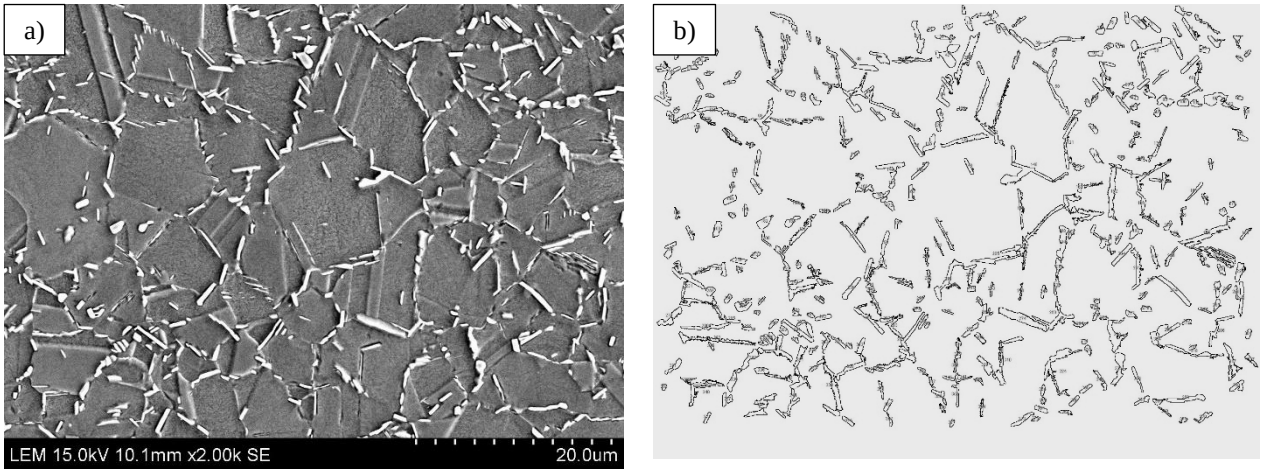

Figure 3: δ micrography (a), Outlines measured (b).

Figure 3 shows one of the micrographs used to the δ phase analysis (a) and the outlines finally obtained (b). The similarity between the images is the key to success of the procedure as a validation of the technique. In the previous

DOI: 10.13009/EUCASS2019-206

table, Table 3, are shown the results of the δ phase size estimation, it is highlighted the mean radius and the circularity as in the previous analysis. However, in this case a lower value can be observed due to the smaller size of the δ phase, around 0.42 µm, compared with the grain size and a minor value of circularity, around 0.36 µm.

3.2. Hastelloy X

In this section, Hastelloy X superalloy is examined. This is a wrought superalloy used in combustion chambers of gas turbine engines. It is a Ni-Cr-Fe-Mo alloy with an exceptional combination of oxidation resistance, manufacturability and high-temperature strength. For high-temperature applications, a thermal barrier coating (TBC) is applied, to protect this part of the engine. In this way, the service temperature of the component can be increased by 300ºC. This barrier is formed by the bond-coat and the ceramic layer, the two of them applied by plasma spray in this case. The aim of this part of the study is to measure both layers and detect some not melted particles, measuring them in order to obtain an estimation of the particle radius used in this technique.

For the measurements of the TBC layers, three different zones of the ceramic layer and the bond-coat have been measured in three micrographs to assure statistical representativity of the results. ImageJ allows to calibrate the pixel size with a known feature thus allowing further real measurements on the image. Two examples of the images used to measure the TBC layers are presented in Figure 4. These are, obtained by different instrumentation, an optical (a) and an electronic micrography (b).

Table 4: Results of TBC layers measurements.

Thickness	Measurements	Overall TBC [µm]	Overall Bond Coat [µm]
Micro 1	3 and 3	474.5	129.6
Micro 2	3 and 3	557.1	126.1
Micro 3	3 and 3	513.2	132.5

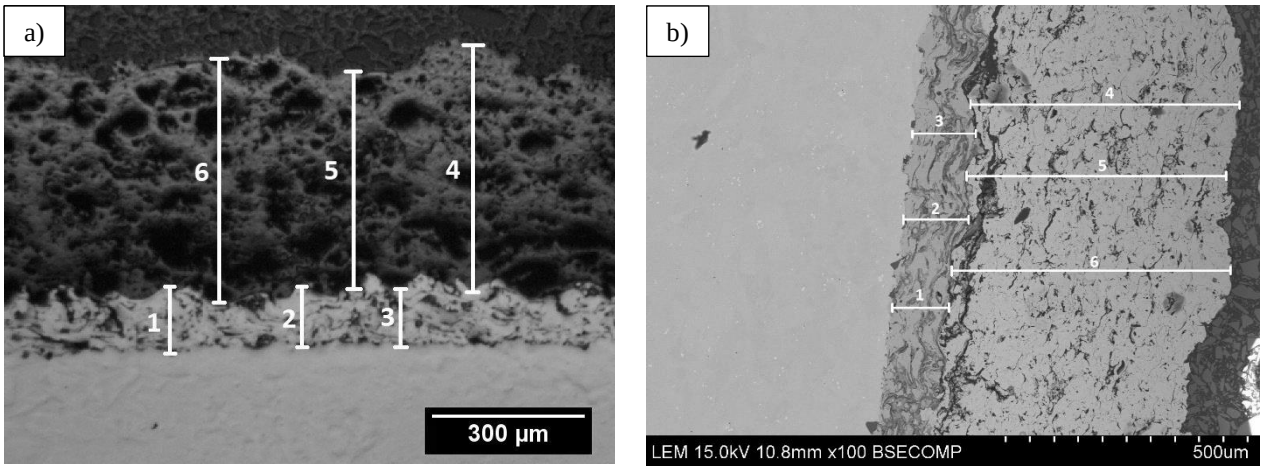

Figure 4: Optical micrography (a), SEM micrography (b).

The results are presented in Table 4, where the overall TBC thickness is shown as 514.9 µm and the bond-coat thickness as 129.4 µm. Both layers are thicker than expected from the theoretical values obtained from the work of Sourmail [22]. However, the studied combustion chamber has been in service, so that can explain the unexpected growth of the layers.

As a part of the study for this alloy, the measurement of the not melted particles has been made. Figure 5 shows the image analysis pursuing this objective. The particles are located with white points (a) and the image was turned into the black and white contrast to improve the analysis of ImageJ.

DOI: 10.13009/EUCASS2019-206

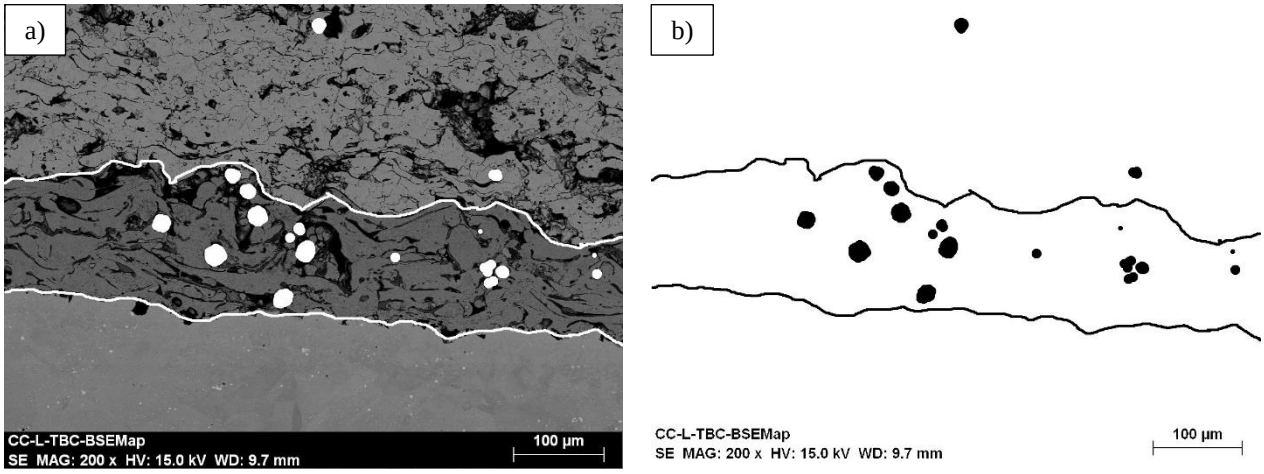

Figure 5: Not melted particles pointed (a) and extracted (b).

The results of the measurements are shown in Table 5. The mean radius is estimated as 8.34 µm and it is also needed to highlight that circularity has a high value, 0.93, because the particles used in plasma sprayed have a spherical shape. In addition, they have a normal diameter distribution between 10 and 60 µm, but it is normal that the smallest can stay solid because of the path strength, maybe they are partially melted particles, or they are in the outside part in the plasma spray so they do not rise the needed temperature [23].

Table 5: Results of the not melted particles measurements.

Not melted Particles	Number of elements	Total area [µm^2]	Overall Area [µm^2]	Mean diameter [µm]	Circularity
Micro 1	18	3929	281.3	16.68	0.93

3.3. Rene 77

In this section the analysed alloy is Rene 77, a casting alloy used for turbine discs and blades of aircraft engines that can work in environments up to 1050ºC, they are normally manufactured by investment casting method [24]. The mechanical properties of this Ni-Co-Cr alloy are not totally controlled by the grain size and its orientation, they are also dependent on the morphology and the amount of precipitates dissolved in the alloy. Because of this, a study of the precipitate distribution and precipitate changes compared to the base alloy one has been performed.

Before the precipitate study, some considerations are needed. We assume that the precipitates observed above on the control surface are representative of the precipitate volumetric fraction. Despite this ideal hypothesis, is the choice for the studies due to the difficulty of knowing the real quantity of precipitate in a determinate volume. This involves maintaining the precipitate determination criteria on the observation surfaces to minimise the dispersion due to errors of assessment.

The first study is the distribution of the precipitate diameter in this alloy. ImageJ is used again to analyse the micrographs obtained from SEM as indicated in Figure 6. In this case, a x2k micrograph, shown in Figure 6 (a), has been chosen to make easier to isolate the cubical precipitate of the alloy (a).

DOI: 10.13009/EUCASS2019-206

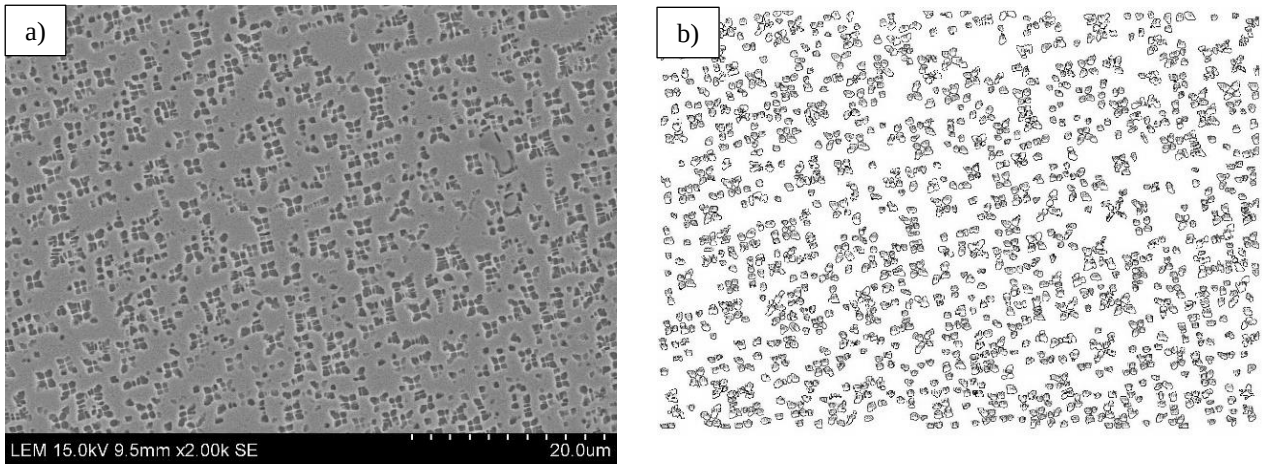

Figure 6: Micrography of Rene 77 (a) and cubical precipitate isolated (b).

With the data obtained from ImageJ it is possible to create a graph showing the diameter distribution of the precipitates, shown in Figure 7. This type of distribution is also found in different metallic alloys such as austenitic or P91 steel [25][26]. They have a lower percentage of precipitate in the case of the steel compared to this alloy, but the distribution has a similar tendency

The second study conducted to this alloy has been the precipitate percentage calculation compared with the matrix percentage. Three different micrographs have been analysed using the open source software, in order to calculate the percentage of cuboidal and spherical separately and check that the precipitate percentage remains constant in all of them, as shown in

Table 6.

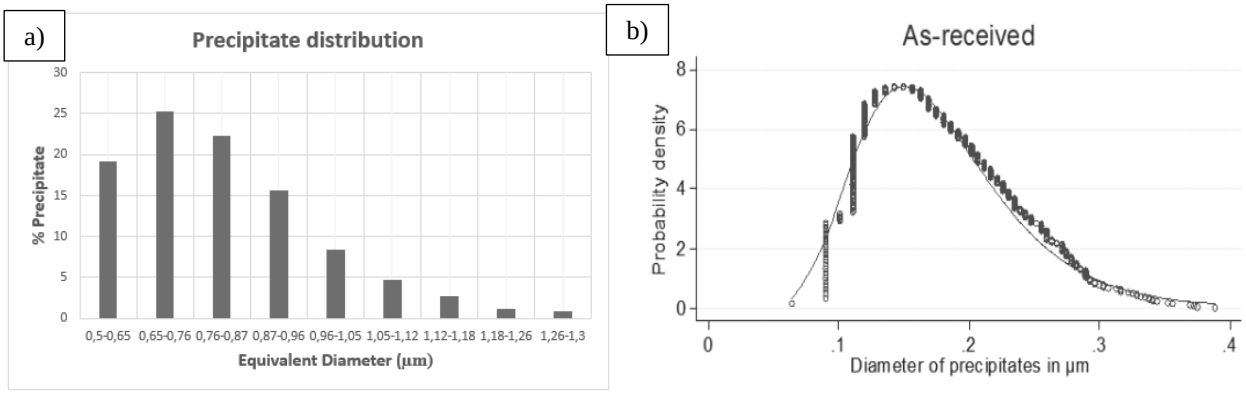

Figure 7: Precipitate distribution of Rene 77 (a) and P91 steel [24] (b).

Table 6: Results of precipitate percentage calculation.

Precipitate	**Cuboidal (%)**	**Spherical (%)**	**Total (%)**
Micro 1	20.9	7,1	28
Micro 2	19,9	7.1	27
Micro 3	19,5	8	27.5

Figure 8 reflects how is the appearance of the different types of precipitates (a) and how accurate can the software get a clear image to be analysed (b). The pair of precipitates can be clearly distinguished in both images.

DOI: 10.13009/EUCASS2019-206

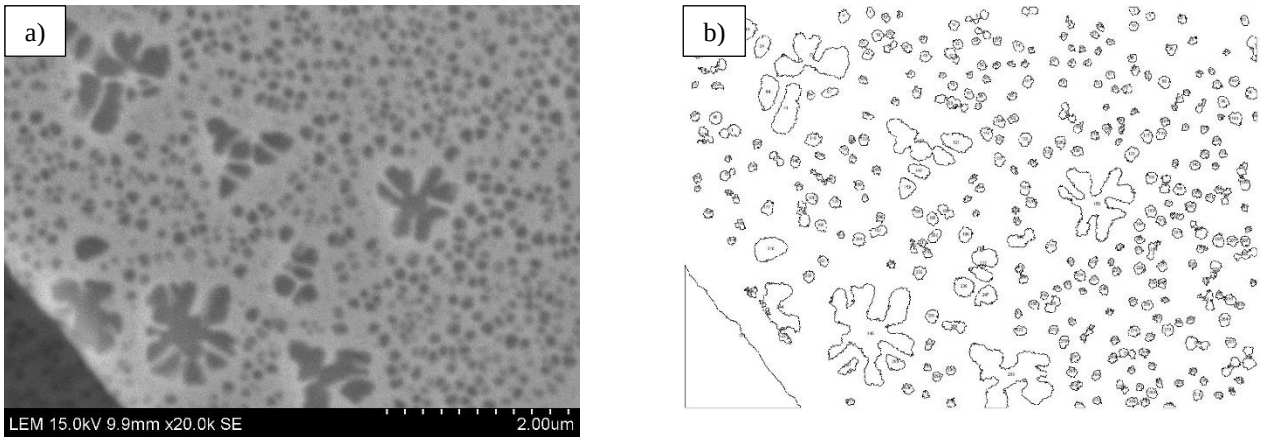

Figure 8: Micrography showing both types of precipitate (a) and the outlines obtained from ImageJ (b).

4. Application of the framework: failure analysis an aerospace component

In this section, the microstructural analysis capabilities of the presented framework are use for the study of the failure analysis of an aerospace component: an auxiliary power unit (APU). The APU under study presents damage concentrated at the airfoil edges a due to reduced thickness in these regions. The componet has been manufactured by casting due to the complex geometry.

The alloy composition of the component (IN738) has been verified by EDX analysis leading to a chemistry close to the nominal one. Due to the lack of knowledge of the initial microstructure, a reference geometry must be defined for the anaylsis. For this purpose, we have compared the microstructures of the failed APU with a second one after service without an airfoil failure. The microstructure of both components has been compared in two regions :

- The area of the blades next to the core of the APU, presenting no damage in both APUs, to validate that both component microstructures are equivalent.
- The area of the blade next to the blade tips were damage is observed for the failed APU. In this way, both healthy and failed microstructure can be compared.

In the next few lines the two different regions of the two APUs are presented and discussed.

4.1. Region near to the core :

4.1.1. Functional APU

The microstructural analysed following the procedure presented in the previous section is presented in Figs. 1-4. The micrographies under study are taken at x5000 to assure a representative number of γ' particles fow this size of precipitates. As observed in Figure 9. The quality and contrast of the image at this magnification is enough to identify accurately the precipitate particles. Several images of different microstructural regions were acquired to assure representative statistical results of the analysis.

The γ' fraction has been extracted from Figure 9-c:

$$f\ (\%) = \frac{\Sigma A_p}{A_{control}} \cdot 100 = \frac{310.6}{897} \cdot 100 \sim 35\% \quad (1)$$

Where:
Ap=Particle area
Acontrol=Total studied area

DOI: 10.13009/EUCASS2019-206

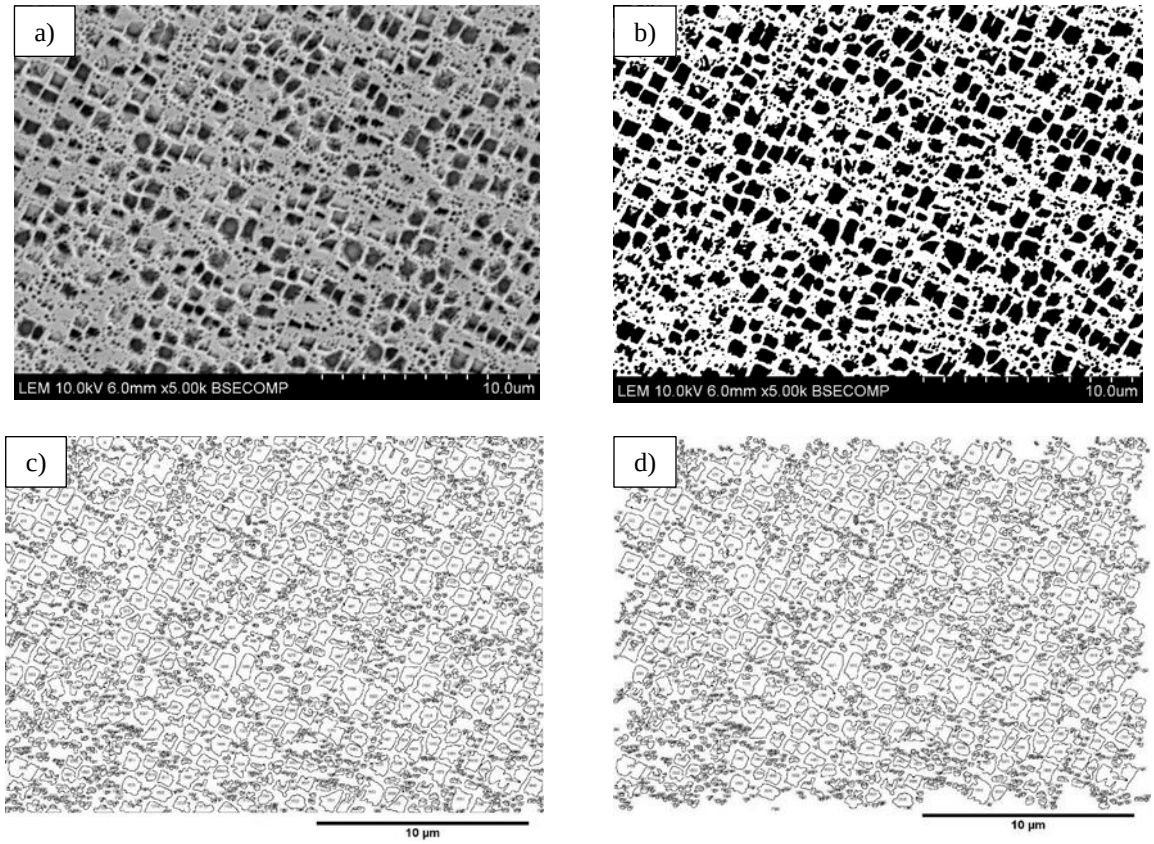

Figure 9: Microstructure of functional APU in not affected zone (a), after GIMP2 treatment (b), Outlines created by ImageJ with incomplete particles in the edge of the image (c) and not including them (d).

The precipitate distribution in Figure 9 was analysed statistically in more detail. The results are presented in Figure 10a) and b) in form of precipitate size distribution and sphericity distribution. The size distributions are calculate using the feret, which is defined as the minimum distance between two parallel tangents to the object.

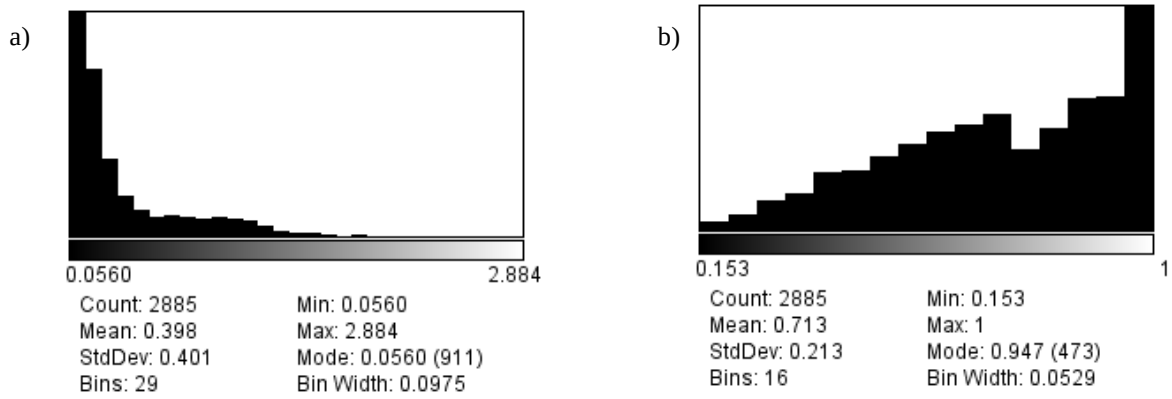

Figure 10: Feret distribution (ImageJ) of image 10-d-(a) and circularity distribution (b)

These results have been further treated to extract the area fraction distribution as a function of the equivalent diameter:

$$Deq\ (\mu m) = \sqrt{\frac{4 \cdot A\ (\mu m^2)}{\pi}} \tag{2}$$

DOI: 10.13009/EUCASS2019-206

Where:
A= Area of the particle
Deq= Equivalent diameter

This is presented in Figure 11. This distribution is more representative of the microstructure as it reduces the effect of the large number smaller particles of the distribution.

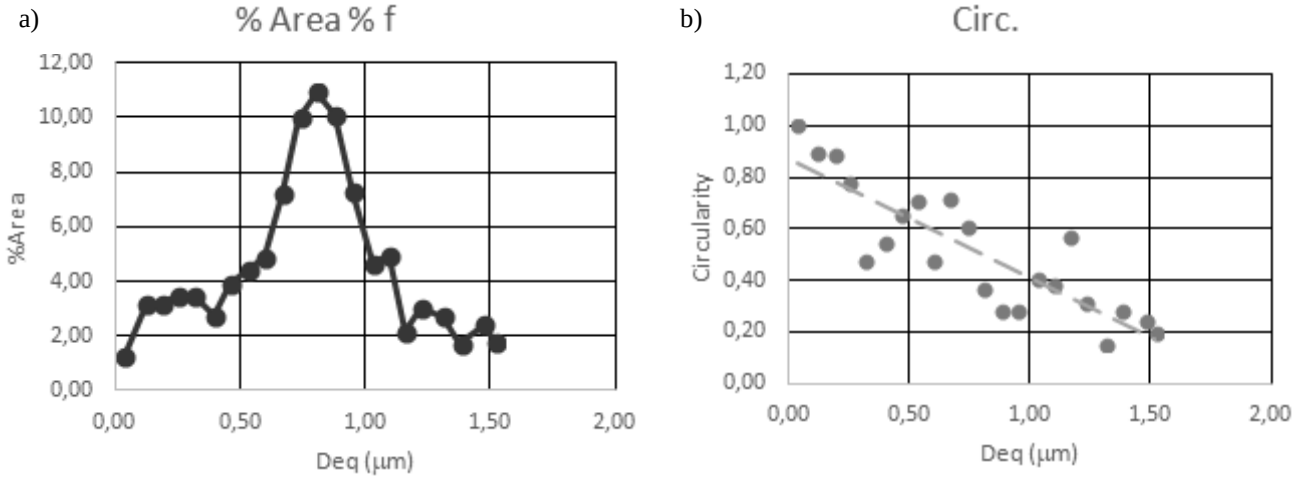

Figure 11: Precipitate size distribution function as % of precipitate area per equivalent diameter (a) and Sphericity of the particles as a function of the equivalent diameter (b).

The sphericty of the precipicates can also be calculated as a function of the equivalent diameter for correlative analysis between size and sphericity. This is presented in Figure 11-b).
From Figure 11-a), it can be observed that most of the particles fall in the region between 0.6 and 1 microns. Similarly, the sphericity of the particles is found to decrease as the particle size increases. This is in agreement with the observed microstructure in Figure 9-a), evolving from circular particles at low equivalent diameters (sphericity=1) to cuboidal shapes for large precipitates.

4.1.2. Failed APU

The same process has been repeated for the failed APU. The processing analysis is presented in Figure 12. The precipitate distribution results and sphericity analysis from ImageJ are shown in Figure 12-c)-d)

The volumentric fraction extracted from Figure 12-c) is :

$$f\ (\%) = \frac{708}{1794} \cdot 100 \sim 39\% \tag{3}$$

The γ' precipitates size distribution as a function of the area fraction is presented in Figure 13-a).

The precipitate sphericity distribution as a function of the equivalent diameter is shown in Figure 13_b).

DOI: 10.13009/EUCASS2019-206

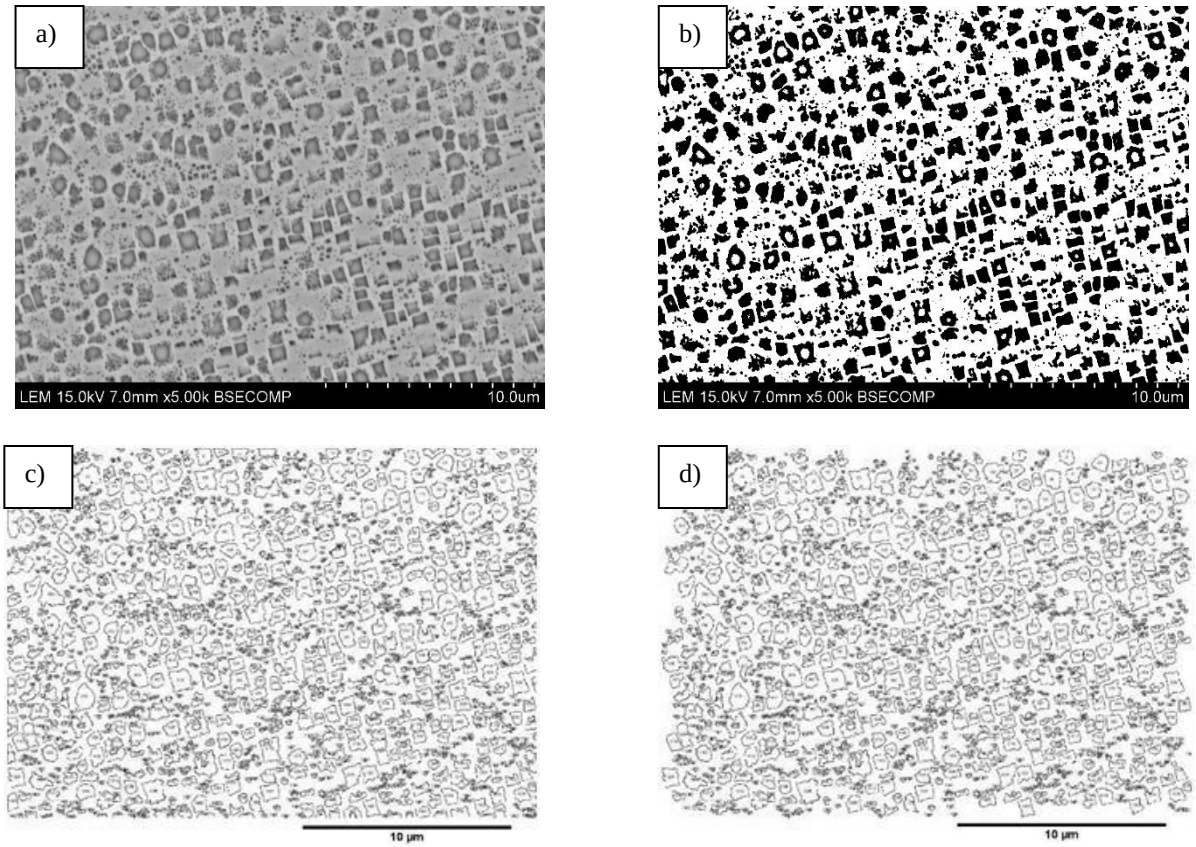

Figure 12 : Microstructure of failed APU in not affected zone (a), after GIMP2 treatment (b), Outlines created by ImageJ with incomplete particles in the edge of the image (c) and not including them (d).

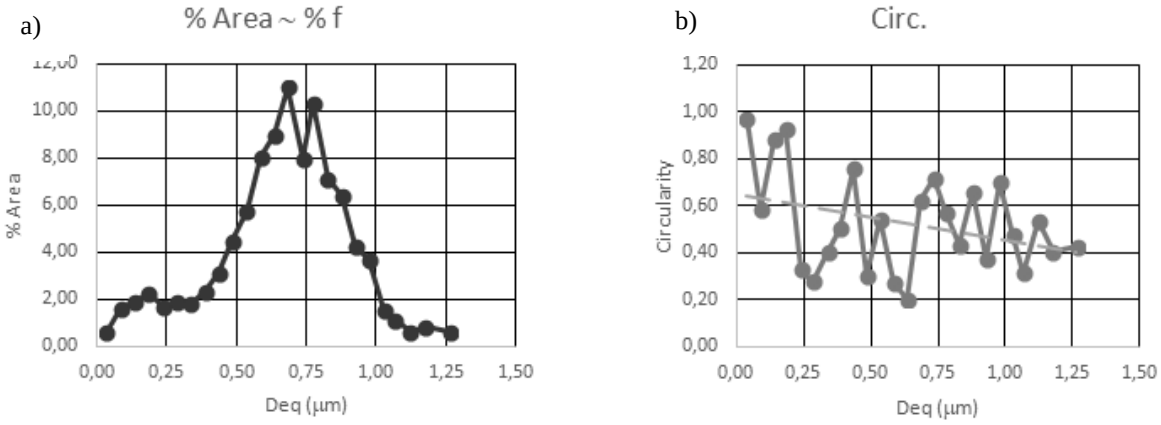

Figure 13: Precipitate size distribution function as % of precipitate area per equivalent diameter (a) and Sphericity of the particles as a function of the equivalent diameter (b).

From the anylised presented, it can be considered that both microstructures from the core regions of both APUs are equivalent. For the case of the equivalent diameter (D_{eq}), the average diameter is slighty smoller for the case of the non-failed APU, see Figure 13-a): D_{eq} is between 0.5-0.9 microns compared with the 0.6-1 micron of the failed APU. The inverse relation between circularity and D_{eq} is maintained for the non-failed APU as indicated inf Figure 13-b).

DOI: 10.13009/EUCASS2019-206

4.2. Region near to the bades tips:

4.2.1. Functional APU

The same process has been repeated for the blade tip region of the non-failed APU. The processing analysis is presented in Figure 14. The precipitate distribution results and sphericity analysis from ImageJ are shown in Figure 15.

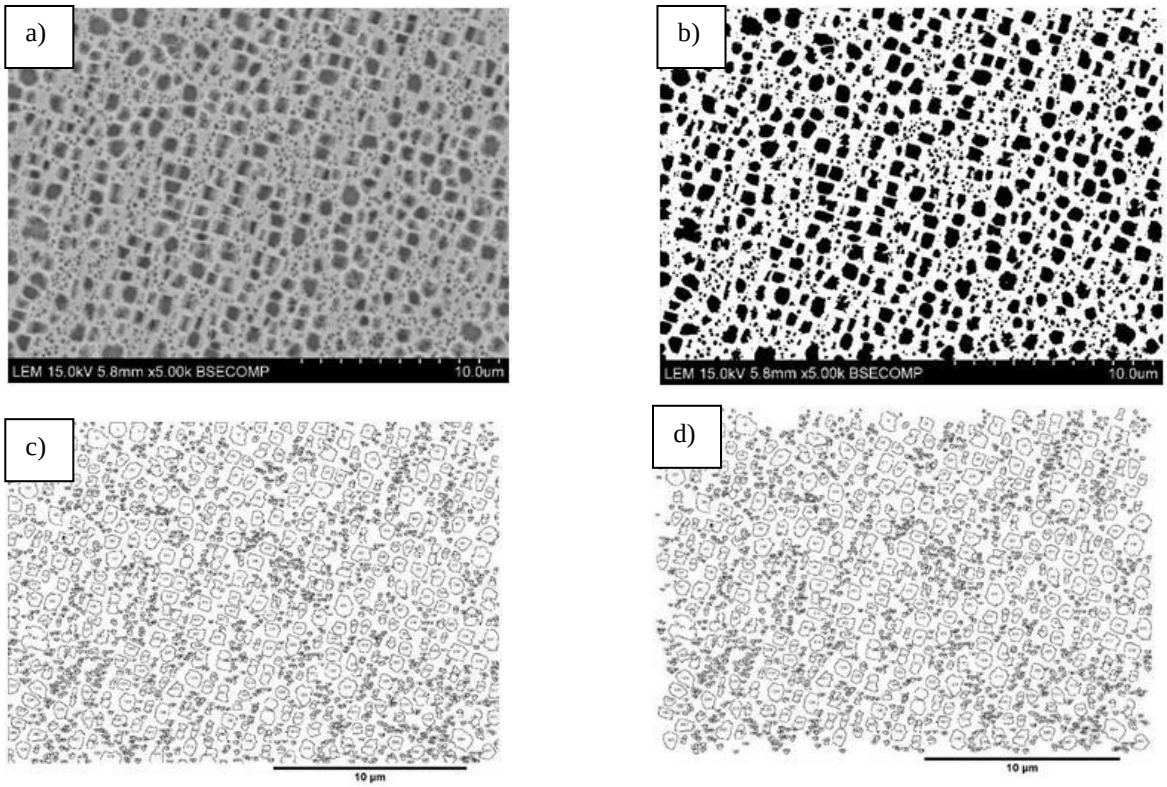

Figure 14: Microstructure of functional APU in not affected zone (a), after GIMP2 treatment (b), Outlines created by ImageJ with incomplete particles in the edge of the image (c) and not including them (d).

The calculated precipitate fraction from Figure 14-c):

$$f\ (\%) = \frac{560}{1346} \cdot 100 \sim 41\% \tag{4}$$

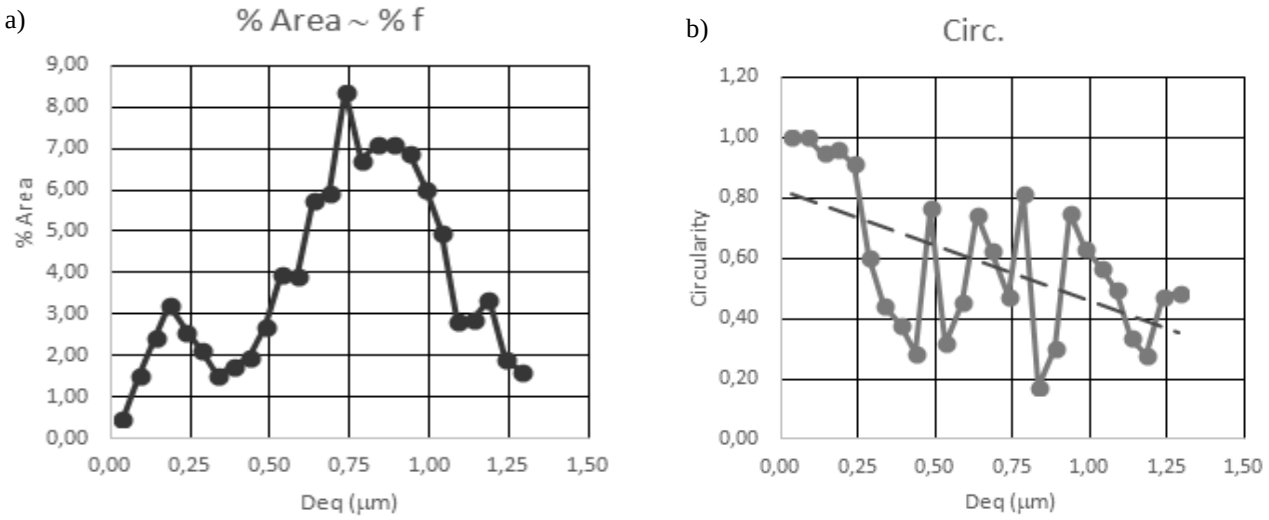

Figure 15 Precipitate size distribution function as % of precipitate area per equivalent diameter (a) and Sphericity of the particles as a function of the equivalent diameter (b).

DOI: 10.13009/EUCASS2019-206

The γ' precipitates size distribution as a function of the are fraction is presented in Figure 15-a and the precipitate sphericity distribution as a function of the equivalent diameter is shown in Figure 15-b.

Both, the volumetric fraction of precipitates and the avergae precipate size are slightly higher than in the core region. However, these are minor changes, maintining similar geometry and size distributions for both regions of the unfailed-APU. The differences in prepitate size can be caused by increased heating in service of this regions of different cooling rates between the core part and the edge of the blades or during the casting process.

4.2.2. Failed APU

Finally, the same analysis has been repeated for the case of the failed APU. The processing analysis is presented in Figs. 25-28. The precipitate distribution results and sphericity analysis from ImageJ are shown in Figs 29-30.

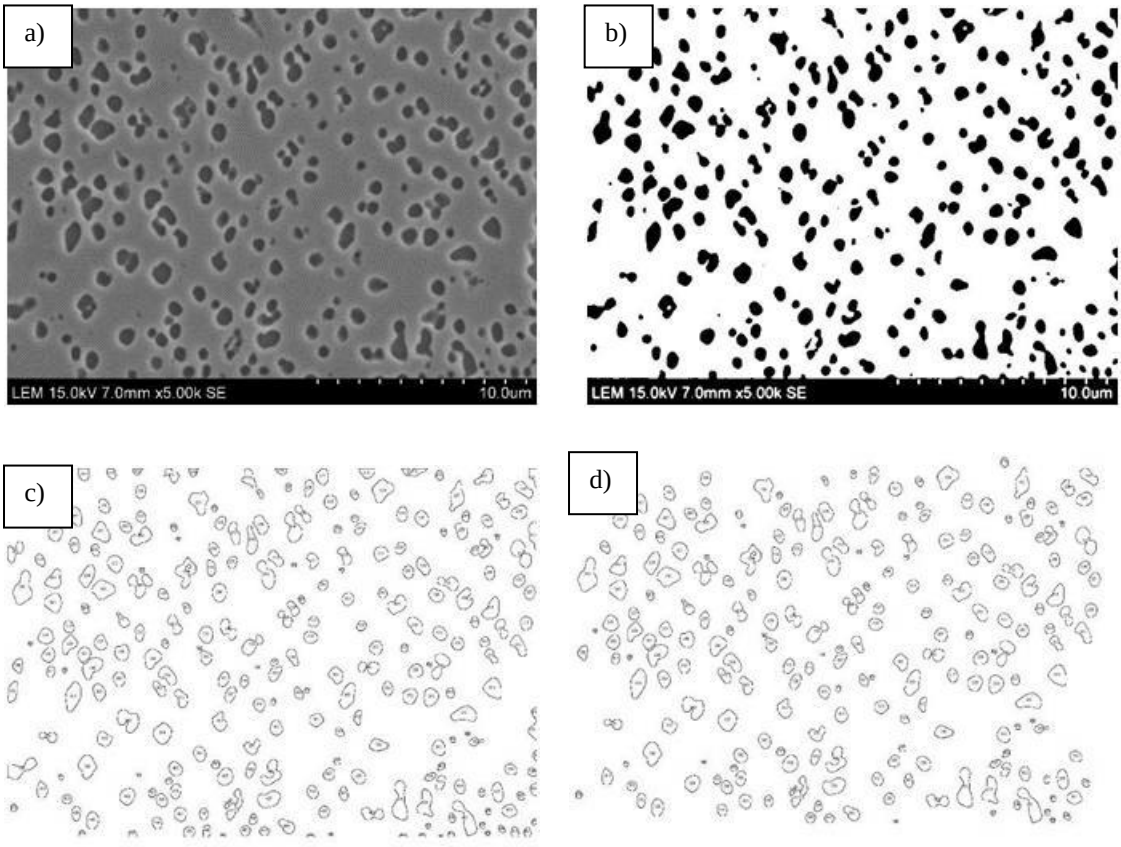

Figure 16: Microstructure of failed APU in not affected zone (a), after GIMP2 treatment (b), Outlines created by ImageJ with incomplete particles in the edge of the image (c) and not including them (d).

The volumetric fraction of precipiates from Figure 16-c) is:

$$f\ (\%) = \frac{139}{897} \cdot 100 \sim 16\% \tag{5}$$

In this case the calculated value (16%) is far from the one observed in the three previous cases (around 50%).
The γ' precipitates size distribution as a function of the are fraction is presented in Figure 17-a).
The precipitate sphericity distribution as a function of the equivalent diameter is shown in Figure 17-b).

DOI: 10.13009/EUCASS2019-206

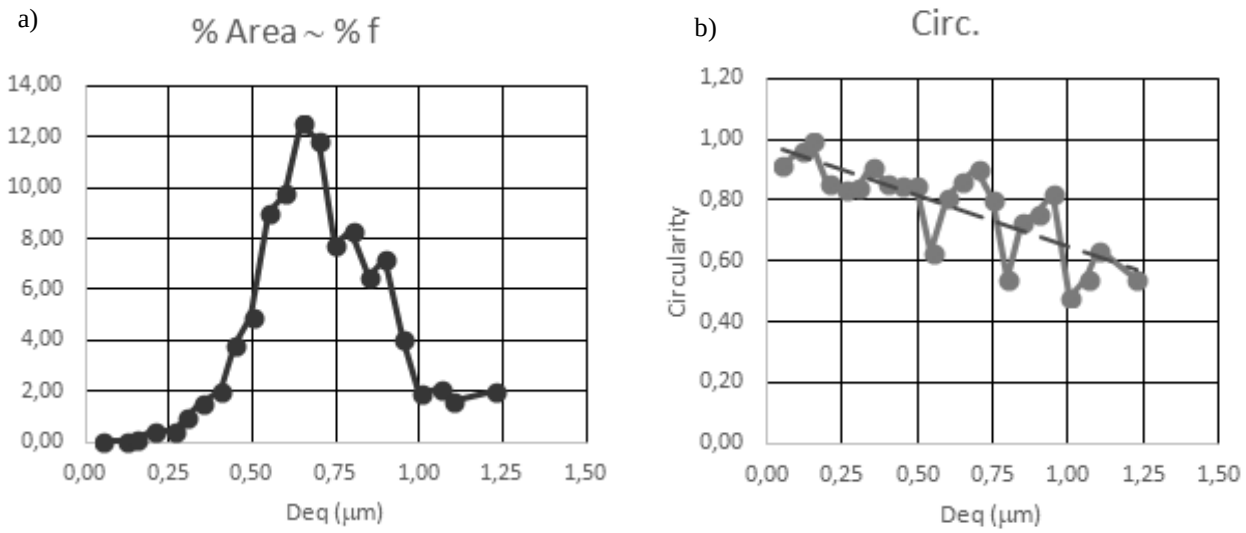

Figure 17 Precipitate size distribution function as % of precipitate area per equivalent diameter (a) and Sphericity of the particles as a function of the equivalent diameter (b).

In Figure 17-a), it can be spotted the absence of precipitates below 0.3 microns of diameter. The previous three cases presented small peaks at around 0.2 microns which mean that for this case (failed APU), the small precipitates have been dissolved in the matrix. This contributes significantly to the reduction of the γ' fraction observed as the small precipitates represent a great proportion of the total number of particles. These small precipitates reduce the dislocation motion into the lattice of the matrix, between cuboidal precipitates; this reduction implies the decrease of the mechanical properties. The precipitate distribution is fairly homogeneous (mostly concentrated between 0.5 and 1 micron). The reduction of sphericity as the precipitate size increases in maintained, though this is less pronounced than in the other three cases. This is an indication that the dissolution process has "round" the cuboidal edges of the precipitates. The elongate ones are the product of the so-called coalescence process of the microstructure observed at high temperatures

5. Conclusions

As informed in the introduction, the aim of this paper is to show the different analysis capabilities of the open-source software (ImageJ). These include grain and delta phase size estimation, layer measurement of thermal barrier coating, failure zone analysis and percentage of precipitate calculation. The Ni-based superalloys that appear in this article have been chosen to show a variety of them and they confirm the accuracy of the method when the alloy and the type of microstructure change.

In the case of Inconel 718, the grain and delta phase size have been estimated with their circularity, showing with the results at the same time the extension and form estimation of them, with a relevant number of analysed elements.
In Hastelloy X a layer measurements have been applied, this technique is possible to apply because of the set scale option that ImageJ has. In addition, two micrographics from optical and electron microscopy have been analysed showing similar results. Finally, the not melted particles in plasma spray technique are located and measured.
Then for Rene 77 a distribution of precipitate diameter is calculated and compared with precipitated percentage, with a huge amount of elements analysed in this study. Another application is the general precipitate percentage with both types analysed separately and applied in a group of micrographics in other to check the conservation of the precipitate in the alloy.

Finally, from the results presented in section 4, the reason for the failure of the APU is the dissolution of the γ' precipitates in service. For the present alloy, the mechanical properties are maintained until 600°C approx. Above this temperature, the precipitates dissolve (Tsolvus) and the mechanical properties provided by them are lost. It is important to notice that the solvus temperature has not been reached as there is still a population of precipitates in the alloy.

From this, it arise the failure cause is the overheating of the APU in service. This might be caused by longer operation times than defined as safe by the manufacturer, due to the high spin rates of these engines in services. In future work,

DOI: 10.13009/EUCASS2019-206

the observed precipitate fraction will be matched to the known microstructural evolution of the alloy as function of temperature to extract the in service conditions leading to the failure of the engine.

6. References

[1] Sajjadi, Seyed Abdolkarim, et al. "Hot deformation processing map and microstructural evaluation of the Ni-based superalloy IN-738LC." Journal of Materials Engineering and Performance25.4 (2016): 1269-1275.
[2] Durand-Charre M. The microstructure of superalloys. Routledge; 2017 Nov 22.
[3] Barba D, Smith TM, Miao J, Mills MJ, Reed RC. Segregation-assisted plasticity in Ni-based superalloys. Metallurgical and Materials Transactions A. 2018 Sep 12:1-3.
[4] Reed, Roger C. The superalloys: fundamentals and applications. Cambridge university press, 2008.
[5] Liu G, Cantó JS, Winwood S, Rhodes K, Birosca S. The effects of microstructure and microtexture generated during solidification on deformation micromechanism in IN713C nickel-based superalloy. Acta Materialia. 2018 Apr 15;148:391-406.
[6] Jun, Tea-Sung, et al. "Local deformation mechanisms of two-phase Ti alloy." Materials Science and Engineering: A 649 (2016): 39-47.
[7] Alabort, E., et al. "On the mechanisms of superplasticity in Ti–6Al–4V." Acta Materialia 105 (2016): 449-463.
[8] Barba, D., et al. "A thermodynamically consistent constitutive model for diffusion-assisted plasticity in Ni-based superalloys." International Journal of Plasticity 105 (2018): 74-98.
[9] Aguirre Cebrián M.V, Martin-Sanz A. Pastor-Caño J.I., Llorca J. "Fco. Javier Llorca Martinez (UPM) Influencia de la composición y microestructura sobre las propiedades mecánicas de aleaciones de wolframio" Anales de la mecánica de fractura 26: 75-80
[10] Van Sluytman JS, Pollock TM. Optimal precipitate shapes in nickel-base γ–γ′ alloys. Acta Materialia. 2012 Feb 1;60(4):1771-83.
[11] Galindo-Nava EI, Connor LD, Rae CM. On the prediction of the yield stress of unimodal and multimodal γ′ Nickel-base superalloys. Acta Materialia. 2015 Oct 1;98:377-90.
[12] Yoon JG, Jeong HW, Yoo YS, Hong HU. Influence of initial microstructure on creep deformation behaviors and fracture characteristics of Haynes 230 superalloy at 900 C. Materials Characterization. 2015 Mar 1;101:49-57.
[13] The jet engine – Rolls Royce 2015
[14] Pollock TM, Tin S. Nickel-based superalloys for advanced turbine engines: chemistry, microstructure and properties. Journal of propulsion and power. 2006 Mar;22(2):361-74.
[15] Smith TM, Bonacuse P, Sosa J, Kulis M, Evans L. A quantifiable and automated volume fraction characterization technique for secondary and tertiary γ′ precipitates in Ni-based superalloys. Materials Characterization. 2018 Jun 1;140:86-94.
[16] Sarosi PM, Viswanathan GB, Whitis D, Mills MJ. Imaging and characterization of fine γ′ precipitates in a commercial nickel-base superalloy. Ultramicroscopy. 2005 Apr 1;103(1):83-93.
[17] Penkalla HJ, Wosik J, Czyrska-Filemonowicz A. Quantitative microstructural characterisation of Ni-base superalloys. Materials chemistry and physics. 2003 Aug 28;81(2-3):417-23.
[18] Szczotok A, Richter J, Cwajna J. Stereological characterization of γ′ phase precipitation in CMSX-6 monocrystalline nickel-base superalloy. Materials Characterization. 2009 Oct 1;60(10):1114-9.
[19] Payton EJ, Phillips PJ, Mills MJ. Semi-automated characterization of the γ′ phase in Ni-based superalloys via high-resolution backscatter imaging. Materials Science and Engineering: A. 2010 Apr 25;527(10-11):2684-92.
[20] Fan Z, Miodownik AP, Tsakiropoulos P. Microstructural characterisation of two phase materials. Materials science and technology. 1993 Dec 1;9(12):1094-100.
[21] Chrapoński J, Szkliniarz W. Quantitative metallography of two-phase titanium alloys. Materials characterization. 2001 Feb 1;46(2-3):149-54.
[22] Sourmail, T. (2008) Coatings for Turbine Blades. Available at: http://www.phase-trans.msm.cam.ac.uk/2003/Superalloys/coatings/index.html.
[23] Fantassi, S., Vardelle, M., Vardelle, A. and Fauchais, P. (1993) 'Influence of the velocity of plasma-sprayed particles on splat formation', Journal of Thermal Spray Technology, 2(4), pp. 379–384. doi: 10.1007/BF02645868.
[24] Zielinska, M. and Sieniawski, J. (2013) 'Surface modification and its influence on the microstructure and creep resistance of nickel based superalloy René 77', Archives of Metallurgy and Materials, 58(1), pp. 95–98. doi: 10.2478/v10172-012-0157-6.
[25] Zieliński, A., Miczka, M., Boryczko, B. and Sroka, M. (2016) 'Forecasting in the presence of microstructural changes for the case of P91 steel after long-term ageing', Archives of Civil and Mechanical Engineering, 16(4), pp. 813–824. doi: 10.1016/j.acme.2016.04.010.
[26] Zieliński, A., Sroka, M., Miczka, M. and Śliwa, A. (2016) 'Forecasting the particle diameter size distribution in P92 (X10CrWMoVNb9-2) steel after long-term ageing at 600 and 650°C', Archives of Metallurgy and Materials, 61(2A), pp. 753–760. doi: 10.1515/amm-2016-0128.